

Predictive Non-linear Dynamics via Neural Networks and Recurrence Plots

L. Lober,* M. S. Palmero,† and F. A. Rodrigues

*Departamento de Matemática Aplicada e Estatística,
Instituto de Ciências Matemáticas e de Computação,
Universidade de São Paulo—Campus de São Carlos,
Caixa Postal 668, 13560-970 São Carlos, São Paulo, Brazil*

(Dated: November 1, 2024)

Predicting and characterizing diverse non-linear behaviors in dynamical systems is a complex challenge, especially due to the inherently presence of chaotic dynamics. Current forecasting methods are reliant on system-specific knowledge or heavily parameterized models, which can be associated with a variety of drawbacks including critical model assumptions, uncertainties in their estimated input hyperparameters, and also being computationally intensive. Moreover, even when combined with recurrence analyses, these approaches are typically constrained to chaos identification, rather than parameter inference. In this work, we address these challenges by proposing a methodology that uses recurrence plots to train convolutional neural networks with the task of estimating the defining control parameters of two distinct non-linear systems: (i) the Logistic map and (ii) the Standard map. By focusing on the neural networks' ability to recognize patterns within recurrence plots, we demonstrate accurate parameter recovery, achieving fairly confident levels of prediction for both systems. This method not only provides a robust approach to predicting diverse non-linear dynamics but also opens up new possibilities for the automated characterization of similar non-linear dynamical systems.

Keywords: Chaos; Neural Network; Recurrence Plots; Logistic map; Standard map.

I. INTRODUCTION

Making accurate predictions in the field of nonlinear dynamical systems can be a challenging task because the evolution of nonlinear relations gives rise to different types of dynamical behavior [1, 2]. Leaving aside induced or inherently stochastic effects, these behaviors can include periodic, quasi-periodic and chaotic dynamics [3]. Periodic motion follows well-defined and regular cycles, whereas quasi-periodic dynamics lack a fixed period but still exhibit ordered motion [4, 5]. Chaotic dynamics, characterized by extreme sensitivity to initial conditions (ICs), evolves unpredictably despite being governed by deterministic rules [6, 7]. Identifying, understanding and especially characterizing this behavior is essential to gain deeper insights into the fundamental nature and properties of dynamical systems of interest.

Parallel to that, developments in the field of neural networks have flourished in the last decade [8], with the introduction of several robust and versatile architectures that allow accurate identification of images in classification problems. Recently, the relevance of neural networks has been highlighted by the 2024 Nobel Prize in Physics, awarded to Geoffrey E. Hinton and John J. Hopfield. Convolutional Neural Networks (CNN) [9, 10] are a subset of feed-forward neural networks that are widely used in image, text and audio recognition tasks, providing a strong foundation for natural language processing techniques that are now state of the art in artificial intelligence, while remaining relevant due to their effectiveness

in many areas. In nonlinear dynamical systems, CNNs have also been shown to identify chaotic dynamics when combined with recurrence analysis, achieving over 92% accuracy [11, 12].

Alongside these neural network advancements, Recurrence Plots (RPs) have become a well-established approach in nonlinear data analysis for visualizing the recurrence of states in dynamical systems [13–15]. Different types of dynamical behavior, such as regular, chaotic or even stochastic motion, produce different visual *recurrence patterns*. [16, 17] and RPs are essentially images composed of white and black pixels representing non-recurrent and recurrent state, respectively, making them particularly suitable inputs for CNNs. These neural networks can then be trained to identify patterns that correspond to the underlying dynamics, offering an automated process for the characterization of different dynamical behaviors. While RPs have been widely used to detect and study chaotic dynamics [18–21], their potential for parameter estimation remains relatively unexplored. By encoding a system's dynamics into a structured visual format, RPs provide a direct method for analyzing behavior and, when combined with CNNs, open up possibilities for inferring system control parameters from recurrence patterns.

In this paper, we propose a methodology that uses CNNs to both classify dynamic behavior and recover control parameters in both one- and two-dimensional nonlinear systems, specifically the logistic and standard maps. By training a CNN on the RPs of these systems, the neural network can predict key control parameters with a fairly high degree of accuracy. Furthermore, the same framework is able to effectively classify different dynamic regimes within the logistic map. Our results demonstrate

* luiza.lober@usp.br

† palmero@usp.br

that CNNs combined with RPs can serve as a powerful numerical approach for characterizing system behavior and identifying the specific parameters that govern it, providing a novel way to apply deep learning to the study of nonlinear dynamics.

The rest of this paper is organized as follows. Section II discusses both the methodology and the models in detail, including the construction of the RPs, the logistic and standard maps and their range of dynamic behaviors, and the architecture of the CNN. Section III presents the results, analyzing the performance of the CNN in both classification and parameter prediction tasks, and discussing the broader implications of these results for the study of nonlinear systems. Finally, section IV concludes the paper with a summary of the results and suggestions for future work, including potential improvements and applications to real-world systems.

II. METHODOLOGY AND MODELS

This section is divided into three sub-sections. Firstly, the process of constructing the RPs is outlined, providing a detailed explanation of how a given percentage of recurrences is determined. Next, the two dynamical systems of interest, namely the logistic and standard maps, are described in detail. Finally, a discussion of the chosen neural network architecture and metrics is presented. Essentially, the whole methodology has been designed to recover the characteristic control parameters of the models through efficient pattern recognition of the RPs.

A. Recurrence Plots

The essence of the proposed methodology relies on the generation of many distinct recurrence plots (RPs), which serve as the fundamental visual representation of the different non-linear dynamical behaviors of interest. It is common to define recurrence if at time t_j , a given trajectory $\mathbf{x}(t_j) \approx \mathbf{x}(t_i)$ approximately returns to a previous state $\varphi(t_i)$, with $t_i < t_j$, meaning it returns to a neighborhood of a past state. Since it is a finite-time analysis, it is worth remarking that $0 < t_i < t_j \leq T$, where T is the trajectory's maximum iteration time.

Depending on the model, its control parameters and initial conditions, different dynamical behaviors may appear and all respective RPs should be constructed considering these differences. Consequently, all RPs were built with a fixed recurrence rate (RR) i.e., the percentage of recurrent points [14], allowing for an unbiased and appropriate comparison among chaotic, periodic, and quasi-periodic dynamics.

The process of building RPs with the same recurrence percentage begins with computing a pairwise distance matrix $D \in \mathbb{R}^{T \times T}$, where each element D_{ij} defined as follows

$$D_{ij} = \|\varphi_i - \varphi_j\|, \quad (1)$$

where $\varphi_i = \varphi(t_i)$, $\varphi_j = \varphi(t_j)$ and $\|\cdot\|$ is a suitable norm. Typically, the Euclidean norm is often used for measuring distances in the respective phase space, which was also employed for this methodology. Note that the i and j are time indexes.

To ensure that the RP has a desired RR , a suitable distance threshold ε must be determined, such that the proportion of points within this distance is equal to the RR . Mathematically, this requirement can be expressed as

$$\frac{1}{N^2} \sum_{i=1}^N \sum_{j=1}^N \Theta(\varepsilon - D_{ij}) = RR, \quad (2)$$

where $\Theta(\varepsilon - D_{ij})$ is the Heaviside step function, which is equal to 1 if $(\varepsilon - D_{ij}) \geq 0$, and 0 otherwise.

The next step to determine ε is to consider the set of all distinct pairwise distances from the distance matrix D , excluding the diagonal elements since $D_{ii} = 0$ by definition. Let the sorted set of these distances be denoted as

$$\{d_1, d_2, \dots, d_M\}, \text{ where } M = \frac{N(N-1)}{2}. \quad (3)$$

The threshold ε is then selected such that approximately $RR \times M$ of the distances are less than or equal to ε . Specifically, for a rate $RR = p$, the particular threshold $\varepsilon = \varepsilon_p$ is chosen such that it corresponds to the $\lfloor p \times M \rfloor$ -th smallest value in the sorted set of distances as follows

$$\varepsilon = \varepsilon_p = d_{\lfloor p \times M \rfloor}. \quad (4)$$

Once the best suited ε is determined, the binary Recurrence Matrix (RM) $R \in \{0, 1\}^{T \times T}$, composed by the elements $R_{i,j}$ can be computed in terms of the distance matrix D as follows

$$R_{ij} = \Theta(\varepsilon_p - D_{ij}). \quad (5)$$

Notice that RM is also a symmetric matrix, as the pairwise distances $D_{ij} = D_{ji}$ for most commonly used norms, ensuring that recurrence relationships are bidirectional. Additionally, while selecting $\varepsilon = \varepsilon_p$, the recurrence rate of this RM is ensured to be $RR = p$.

Finally, the visual representation of the RM is the RP of interest. Typically, RPs represent each zero entry ($R_{ij} = 0$) of the RM as a white pixel, while each 1 entry ($R_{ij} = 1$) is represented by a black pixel. To ensure that each recurrent point is represented by a unique pixel, the desirable resolution of an RP is $T \times T$ pixels, where T is the maximum iteration time of the dynamics being analyzed. This resolution ensures that the recurrence patterns are accurately represented without overlap, making it easier to visually distinguish between different dynamic behaviors. The optimal choice of resolutions and T is further explored in the appendix A.

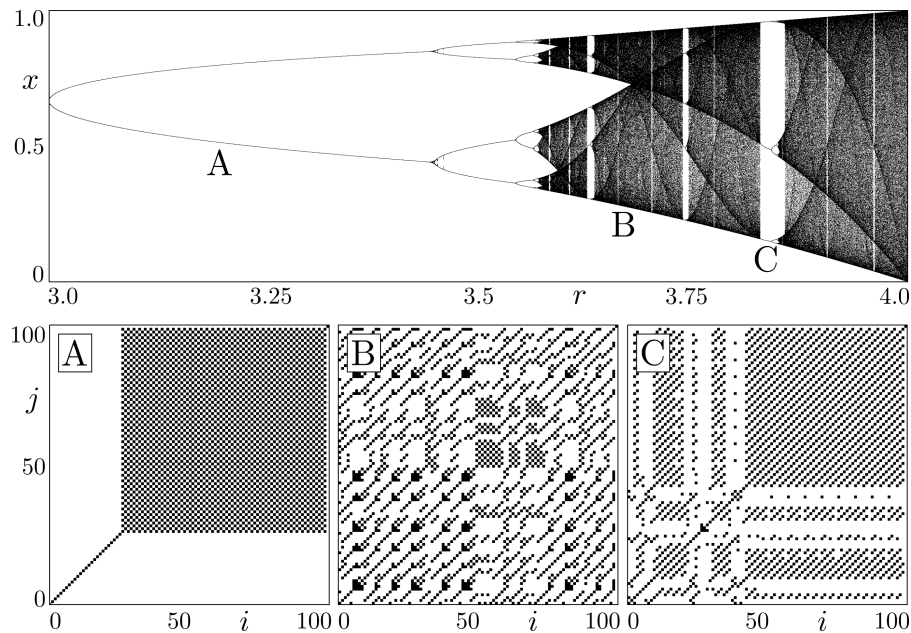


FIG. 1. (Upper panel) Typical bifurcation diagram of the Logistic map; (Lower panels) Three RPs from different values of the control parameter r . For A, the pair IC and parameter was set ($x_0 = 0.1, r = 3.20$) – permanent periodic dynamics; In B, the pair was ($x_0 = 0.1, r = 3.70$) – chaotic dynamics; In C, ($x_0 = 0.1, r = 3.85$) – chaotic, but close to stability islands. RPs were build from $T = 100$ and fixed $RR = 20\%$.

B. Models

The two dynamical systems studied in this paper are well known nonlinear maps. The first, introduced by Lorenz in the 1960s [22] and popularized by May in 1976 [23], the logistic map, is a standard example of how complex and chaotic behavior can arise from a simple one-dimensional nonlinear equation, with applications ranging from population dynamics, pseudo-random number generators to bifurcation theory [1].

In addition to the logistic map, the Chirikov standard map, an example of a two-dimensional near-integrable Hamiltonian system, was also selected. First conceptualized in the 1970s in the context of plasma physics [24, 25], the standard map exhibits a rich variety of dynamical behaviors, in particular Hamiltonian chaos, making it an ideal subject for this investigation.

The next subsections provide a detailed explanation along with examples of the dynamics presented by the logistic and standard maps.

1. The Logistic map

As briefly introduced earlier, the logistic map brings its non-linearity from a simple quadratic term as follows

$$x_{t+1} = rx_t(1 - x_t), \quad (6)$$

where the defining control parameter r in the range of $[0,4]$ produces values of x_t bounded on $[0,1]$, with diver-

gences presented when $r > 4$. Here, it will be restricted to the former range.

The logistic map can have several behaviors according to the values taken by r , which are briefly described below.

- $0 < r < 1.0$: Independently of the initial conditions, $\lim_{t \rightarrow \infty} x_t \rightarrow 0$;
- $1.0 < r < 2.0$: $\lim_{t \rightarrow \infty} x_t \rightarrow \frac{r-1}{r}$, also without regard to the initial conditions;
- $2.0 < r < 3.0$: Similar to the previous range, however presenting fluctuations around the final value before convergence;
- (A) $3.0 < r < 3.56995$: Permanent oscillatory behavior is observed, with the number of modes of oscillation depending on r ;
 - (A1) $3.0 < r < 3.44949$: The dynamics oscillates between two values;
 - (A2) $3.44949 < r < 3.54409$: Four oscillatory solutions are observed;
 - (A3) $3.54409 < r < 3.56995$: Oscillations increase even further, allowing for κ values, with κ even and increasing according to r .
- (B) $3.56995 < r < 3.82843$: onset of chaos;
- (C) $3.82843 < r < 4.0$: certain values of r result in the emergence of *islands of stability*.

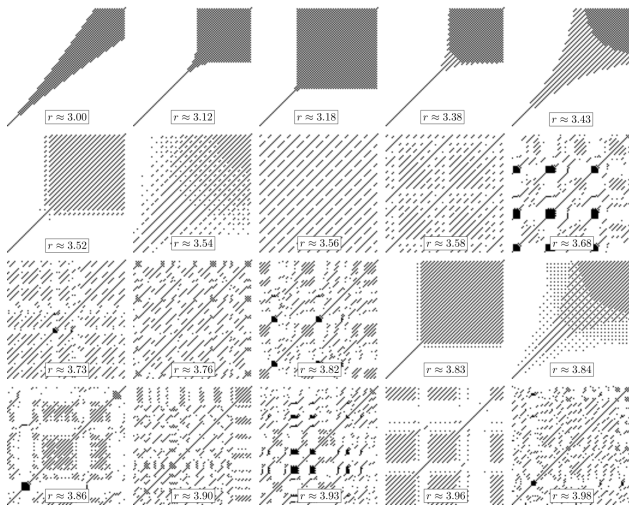


FIG. 2. Twenty different dynamical behaviors displayed by their respective RP constructed from the dynamics of the Logistic map. All RPs were built from $T = 100$ iterations and fixed $RR = 20\%$. All correspondent approximated value of the parameter r is displayed inside each RP.

For this study, data generation and analysis were restricted to values $r \in [3.0, 4.0]$, and the previous ranges will be employed to define multiple labels (A1, A2, A3, B and C) for the upcoming classification task.

Figure 1 shows the classical bifurcation diagram along with three distinct RPs, each considering different values of r that properly display the diversity of dynamical behaviors. In agreement with the discussions presented at Sec. II A and Appendix A, all RPs from the dynamics of the logistic map were constructed considering a fixed $RR = 20\%$, and $T = 100$ iterations.

Since it is important to produce multiple distinct RPs, knowing that neural networks benefit greatly from large volumes of samples, a thorough numerical experiment was conducted to extract as many behaviors from the map as possible. The range $r \in [3.0, 4.0]$ was uniformly divided into 10^4 values, generating the same 10^4 different RPs, each differing in the value of r up to the fifth decimal place. The parameters of the dynamics, namely the IC x_0 , and the maximum iteration time T were set to 0.1 and 100 respectively. The RP parameters, including the RR and resolution, were set to 20% and 100×100 respectively. A sub-sample of this analysis, consisting of 20 RPs, is shown in Fig. 2, and all 10^4 images were compressed into a Graphic Interchange Format (GIF) made available in the supplemental material.

It is worth remarking that the initial periodic behaviors, displayed by the first row of RPs in Fig. 2, may exhibit patterns that do not necessarily match the typical appearance of fully periodic RPs [13, 14]. This is because, instead of using a predefined threshold distance ε , these RPs were constructed with a fixed RR . Hence, as periodic dynamics presents multiple recurrences, especially for $r \approx 3.0$, the RP is proportionally filled by

points until reaching the desired $RR = 20\%$. It is also interesting to observe the diversity of patterns within the chaotic regime, followed by an unambiguous periodic behavior produced by the stability islands for $r \approx 3.83$, before returning to chaos as r increases.

2. The Standard map

The Standard map, also known as the Chirikov Standard map, can be used to describe the motion of a particle constrained to a movement on a ring while kicked periodically by an external field. It is possible to define a symplectic non-linear discrete map that gives the particle's generalized position q and momentum p for the $(t + 1)^{th}$ iteration by the following equations

$$p_{t+1} = p_t + k \sin(q_t) \quad \text{mod } (2\pi), \quad (7)$$

$$q_{t+1} = q_t + p_{t+1} + \pi \quad \text{mod } (2\pi), \quad (8)$$

where the parameter k controls the intensity of the non-linearity and the added term $+\pi$, on the Eq. (8), is to centralize the main island on the phase space. It is also important to note that this is an area-preserving map since it comes from a Hamiltonian system, and the determinant of its Jacobian matrix is equal to unity.

The characteristic mixed phase spaces of the Standard map are shown in Fig. 3. These phase spaces are said to be mixed as chaotic areas can coexist with periodic regions [5]. As illustrated by the gray points in the background, depending on the pair of ICs (q_0, p_0) a given trajectory may fill invariant spanning curves i.e. curves that span throughout the whole phase space; fill periodic structures within stability islands, also known as Kolmogorov-Arnold-Moser (KAM) islands [4]; or fill the chaotic area.

As predicted by the theory of near-integrable Hamiltonian systems, chaos emerges in the vicinity of unstable fixed points as the control parameter increases [26]. It can be observed that Eqs. (8) and (7) have a stable fixed point at (π, π) and an unstable one at $(0, \pi)$ or $(2\pi, \pi)$ due to the modulo (2π) condition. Hence, for sufficiently large values of k , the region in the near surroundings of $(0, \pi)$ will always be filled by chaotic orbits, as evidenced by the inset zoom on the first panel of Fig. 3, where $k = 0.3$. Figure 3 also displays the growth of the chaotic region for larger parameter values, namely $k = 0.9$ and $k = 1.8$ for the remaining upper panels.

The second panel of Fig. 3, shows a particular phase space configuration close to an important topological transition that happens in the Standard map. For the critical value $k = k_c = 0.971635$, the last invariant spanning curve is destroyed and the map transits from local to global chaos [27, 28], where for a sufficient long evolution, any chaotic orbit may fill out the whole phase space, with the only exception to the inside of the KAM islands embedded to what is now called the *chaotic sea*. This configuration is exemplified by the third panel of Fig. 3.

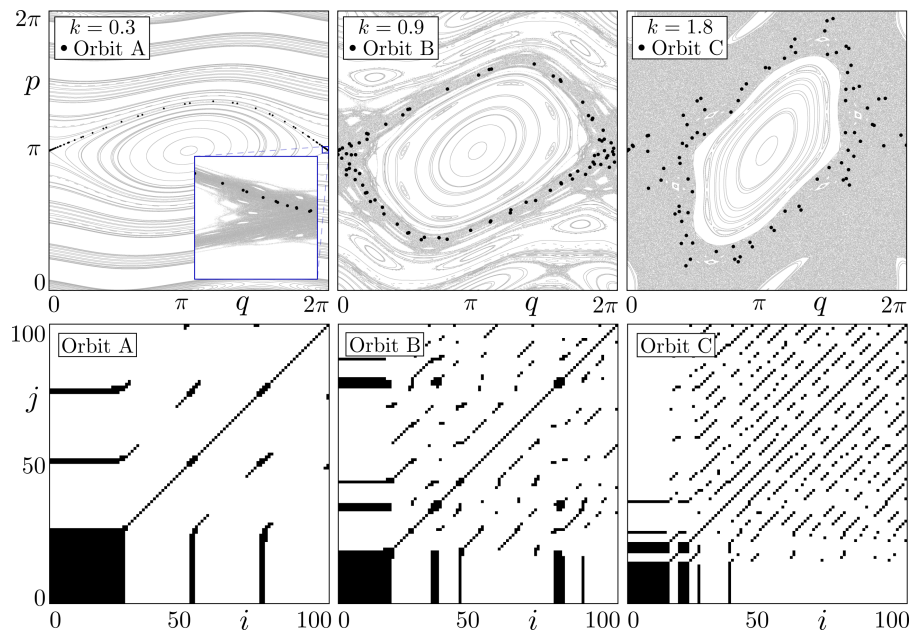


FIG. 3. (Upper panels) Phase spaces of the Standard map (gray background) for three increasing values of the control parameter k , along with a chosen chaotic orbit depicted by the black points; (Lower panels) RPs of each of these orbits. Orbits A, B and C were evolved from a fixed IC $(q_0, p_0) = (10^{-9}, \pi)$, while the RPs were build from $T = 100$ and fixed $RR = 10\%$.

In addition to the mixed phase spaces, the lower panels of Fig. 3 also display three RPs associated with orbits A, B and C. These particular trajectories, represented by the black points on their respective phase spaces, are chaotic orbits initiated from a fixed IC $(q_0, p_0) = (10^{-9}, \pi)$, meaning that they start extremely close to the unstable fixed point. Indeed, at the beginning of their dynamical evolution, the influence of the fixed point is still dominant, as evidenced by the initial black squares in all RPs. Nevertheless, since it is a neighborhood of an unstable fixed point, the chaotic behavior eventually emerges as the orbits lose stability and explore the available chaotic areas.

Following the approach used for the Logistic map in the previous subsection, Fig. 4 shows the diversity of RPs constructed from various chaotic trajectories in the Standard map. This figure also employs ICs with trajectories fixed as $(q_0, p_0) = (10^{-9}, \pi)$, while the control parameter k was changed thoroughly within the range $[0.1, 2.0)$. Similar to the Logistic map, this range was uniformly divided into 10^4 values, generating 10^4 different RPs, each differing in the value of k up to the fourth decimal place. The RP parameters, including the RR and resolution, were set to 10% and 100×100 respectively. While Fig. 4 shows twenty examples of these RPs with increasing values of k , all 10^4 images were compressed into a GIF, which is also available in the supplementary material.

It is important to point out that these sets of RP images, exemplified by Figs. 2 and 4, provide effective visual representations of various finite-time dynamical behaviors. In this sense, understanding all the recurrence patterns associated with these RPs is essential to their

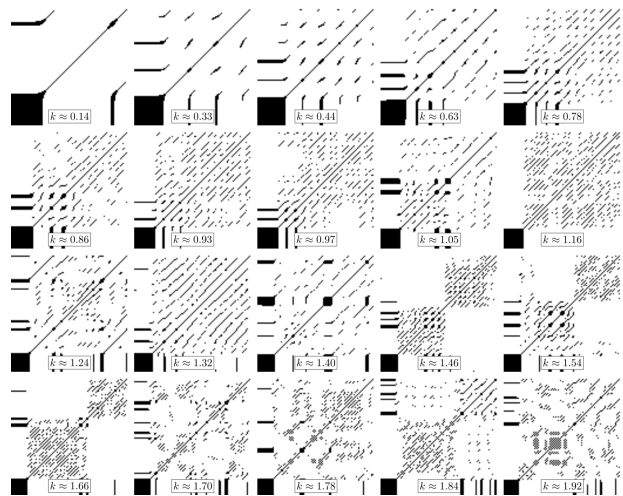


FIG. 4. Twenty different chaotic behaviors displayed by their respective RP constructed from the dynamics of the Standard map. All RPs were build from $T = 100$ iterations and fixed $RR = 10\%$. All correspondent approximated value of the parameter k is displayed inside each RP.

characterization. To achieve this, a convolutional neural network is trained to effectively obtain the characteristic control parameters associated with these dynamical behaviors.

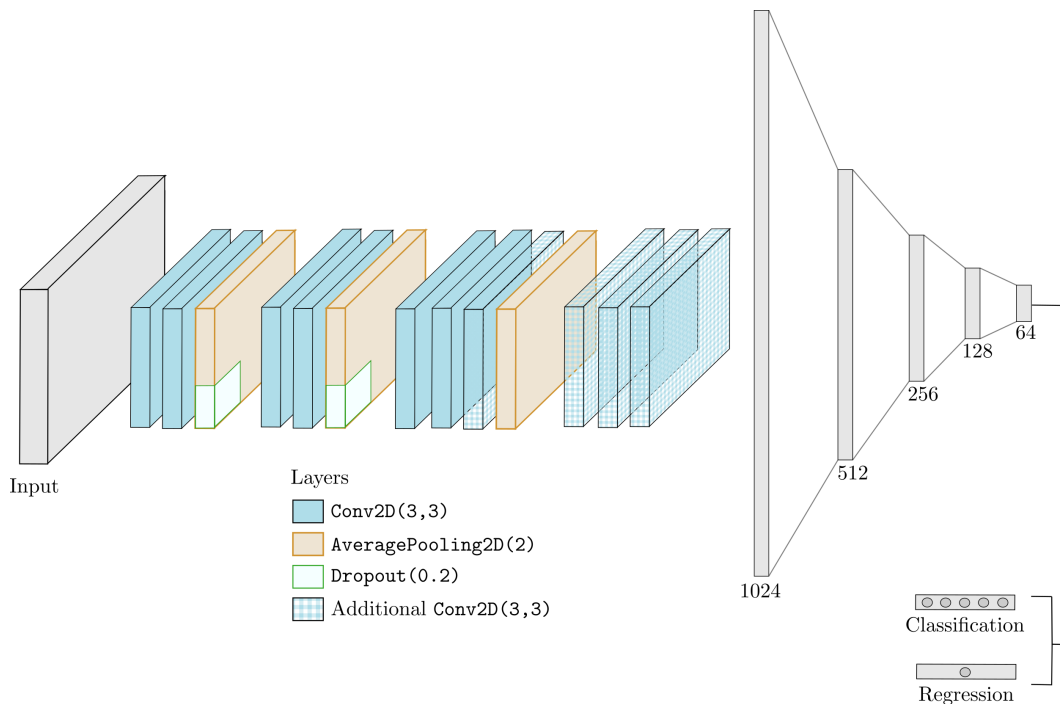


FIG. 5. General architecture of the CNN implemented. Layers indicated in solid colors were used for both dynamics, with the hatched blocks employed solely for the dynamics of the Standard map, and dropout used only for the Logistic map.

C. CNN and metrics

The architecture of all convolutional neural networks employed in this investigation was defined as shown in Fig. 5, using the structure available at TensorFlow [29]. As for the choice of hyperparameters, the model consists of: 100 batch size; Conv2D(3,3) for each convolutional layer; AveragePooling2D(2) as the pooling layers; ReLu() as the activation function with Adam as chosen optimizer. Root Mean Squared Error (RMSE) and Categorical Cross Entropy are used as loss functions for regression and classification tasks respectively. The training employed 300 maximum epochs, allowing for early stopping with the criteria of interruption being 0.001 and 20 epochs.

In terms of the amount of samples generated that are being used as inputs, the main models had access to 4×10^4 unique RPs for the training step, which were composed of 10^4 uniformly chosen values of r and k for four sets of ICs: $x_0 = 0.10, 0.25, 0.50$ and 0.75 for the Logistic map; $(q_0, p_0) = (\delta \times 10^{-\gamma}, \pi)$ where $\gamma = 8$ is fixed and $\delta = 2, 4, 6$ and 8 for the Standard map. Different values of γ were also considered and are further explained in Appendix A.

As a way to quickly access the control parameters in the training stage, those are saved while naming each sample, and latter being imported to the respective train and test vectors while loading the images to the models.

Each network was trained independently in two different RP train sets: the first set containing data from the

Logistic map generated with parameters $r \in [3.0, 4.0]$, and the second with r immediately after the onset of chaos; while for the Standard map, $k \in [0.1, 0.971635]$ and a larger range $k \in [0.1, 2.0]$ were used to generate the data sets for this dynamic. The amount of samples, originated from the same sets of ICs, remained constant for the analysis focused on the onset of chaos and $k < k_c \approx 0.971635$, resulting in larger training sets for these regions where the chaotic behavior is predominant.

When evaluating the trained neural networks, 10^3 non-interloping samples were generated as the hold-out test set by randomly sorting the defining parameter of each map and fixing the IC $x_0 = 0.4$ (Logistic) and $(q_0, p_0) = (5 \times 10^{-8}, \pi)$ (Standard).

The evaluation of the performance of the trained models used the following metrics: the weighted f_1 score was employed to assess the accuracy of predictions across the defined intervals of r to which the testing RP samples belonged in the Logistic map. For the regression tasks, a point-wise error, based on the absolute differences between the actual and predicted parameter values, was used to evaluate the estimated r and k values for the Logistic and Standard maps, respectively.

Additionally, considering an acceptable margin m , a given prediction can be categorized as follows:

$$C_i(m) = \Theta(m - |y_i - \hat{y}_i|), \quad (9)$$

where y_i and \hat{y}_i represent the actual and predicted parameter values for sample i , respectively. The Heaviside

TABLE I. Accuracy presented for the classification task on the logistic map, employing f_1 score as the metric; and the regression task, using $RMSE$, both for the test set, for each interval of r as described in Sec. II B 1.

Class	RMSE	$c(0.1)$	$c(0.01)$	f_1 score	support
3.0 < r < 4.0					
(A1)	0.0179	99.8%	47.4%	0.997	439
(A2)	0.0181	100%	22.6%	1.000	93
(A3)	0.0185	100%	40.9%	1.000	22
(B)	0.1195	66.0%	7.9%	0.903	265
(C)	0.1162	59.7%	15.5%	0.871	181
weight. avg.	0.0626	-	-	0.966	1000
3.56 < r < 4.0					
(A3)	0.0069	100%	82.35%	0.971	17
(B)	0.0459	95.07%	24.34%	0.965	608
(C)	0.0722	86.93%	16.00%	0.947	375
weight. avg.	0.0551	-	-	0.989	1000

step function ensures that if $|y_i - \hat{y}_i| < m$, $C_i = 1$, indicating that the predicted value is within the acceptable margin m from the actual value; otherwise, $C_i = 0$, representing an incorrect prediction.

The total number of predictions within the m -tolerance is then given by $C(m) = \sum_{i=1}^N C_i(m)$, where N is the total number of test samples. Furthermore, the percentage of correct predictions is defined as

$$c(m) = \frac{C(m)}{N} \times 100\%, \quad (10)$$

where, in practical terms, if $m = 0.01$, the percentage $c(0.01)$ expresses how accurately the NN can predict the parameter value up to the third decimal place.

The next section is dedicated to presenting and explaining the main results of the proposed methodology.

III. RESULTS AND DISCUSSIONS

The first set of results comes from applying the aforementioned methodology to the Logistic map. 4×10^4 RPs, representing distinct non-linear dynamical behaviors from Eq. (6), were constructed considering fixed $RR = 20\%$ and $T = 100$. The task of the trained NNs is to predict both the value and range of the characteristic control parameter r , respectively through a regression and classification task. Table I presents the outcome of the models for the hold-out test samples.

Notice that the weighted accuracy obtained, shown in column “ f_1 score” for training the NN almost exclusively on the chaotic region is higher than currently reported in literature [9, 10], and also improved while comparing with RPs originated from $r \in [3.0, 4.0]$. As for the regression results displayed on columns “RMSE, $c(0.1)$ and $c(0.01)$ ”, the same improvement on characterizing chaotic dynamics is observed when focusing solely on the

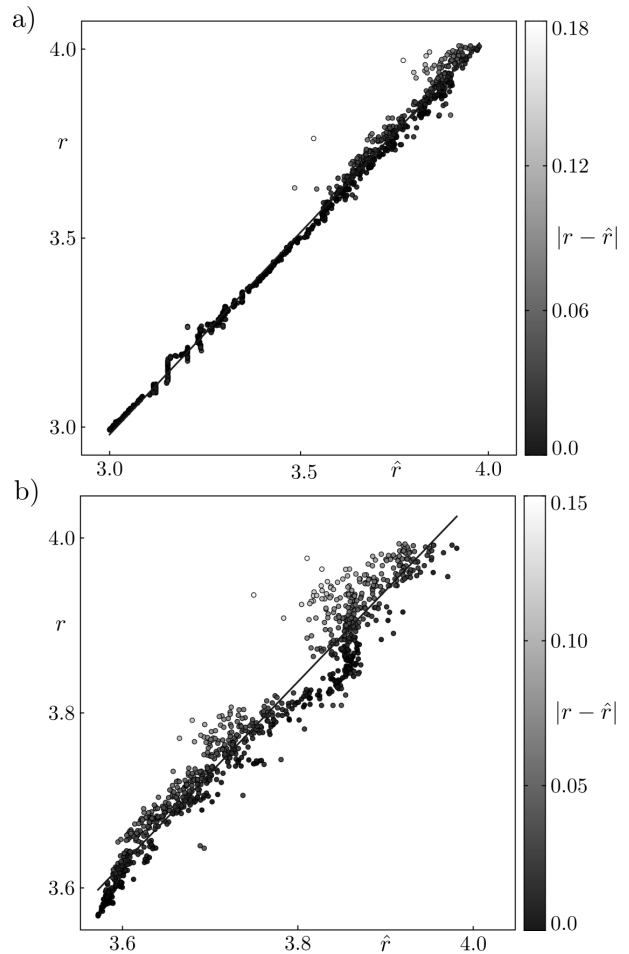


FIG. 6. Predicted values (\hat{r}) compared to actual parameter (r) values of the test set from the Logistic Map in the regression task. The colour axis illustrates the dispersion on the absolute difference $|r - \hat{r}|$ in both cases: (a) $r \in [3.0, 4.0]$ and; (b) $r \in [3.56, 4.0]$.

chaotic region, where at least 86.93% of predicted parameters \hat{r} are precise within two decimal places to the actual parameter r .

Figure 6 illustrates the regression results for the Logistic map. From Fig. 6 (a), it is clear that the proposed NN is successfully predicting the parameter values, especially before the onset of chaos at $r \approx 3.57$. After that, the predictions weaken as the chaotic regime dominates the dynamics. To further investigate, the same amount of RP samples was used to train the NN, solely considering $r \in [3.56, 4.0]$. The regression for this specific range is shown in Fig. 6 (b).

In comparison to (a), Fig. 6 (b) shows an inferior agreement between the predicted and actual parameter values. This is due to the fact that the chaotic regime may present many distinct recurrence patterns, as earlier evidenced by the RPs within this range in Fig. 2. These many faces of chaotic behavior are expected for a finite-time analysis, making the predictions more challenging, and consequently lowering the NN accuracy. Addition-

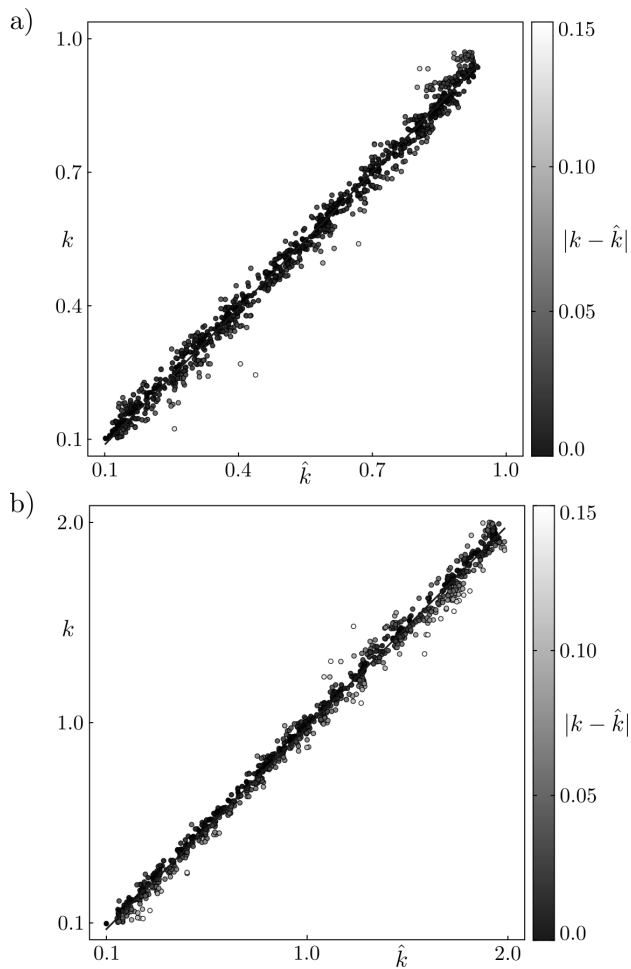


FIG. 7. Predicted values (\hat{k}) compared to actual parameter (k) values of the test set from the Logistic map in the regression task. The color axis illustrates the dispersion on the absolute difference $|k - \hat{k}|$ in both cases: (a) $k \in [0.1, k_c)$ and; (b) $r \in [0.1, 2.0)$.

TABLE II. RMSE and overall precision for the regression task for RPs generated from the Standard map.

k interval	RMSE	$c(0.1)$	$c(0.01)$
$[0.1, k_c)$	0.0273	99.4%	47.8%
$[0.1, 2)$	0.0742	85.0%	14.6%

ally, regions between $3.8 < r < 3.9$, where the agreement is even less accurate, correlate to the rise of periodic and quasi-periodic behaviors due to islands of stability of said region. Yet, as observed in Tab. I, this region is successfully classified, presenting relatively high f_1 score.

Considering the Standard map, Tab. II summarizes the performance of the trained NN with the RPs from the different non-linear dynamical behaviors of Eqs. (7) and (8). Again, 4×10^4 RPs were constructed considering $T = 100$, but now $RR = 10\%$. In contrast to the Logistic map, all RPs of the Standard map represent chaotic behaviors, specifically different finite-time trajectories in

Hamiltonian chaos. In that sense, employing the process outlined in Sec. IIA for a relatively high RR may require longer computational simulations, so $RR = 10\%$ was chosen. Additionally, since only chaotic behavior is analyzed, classification tasks were neglected.

It is important to emphasize that by selecting trajectories with specific ICs, namely $(q_0, p_0) = (\delta \times 10^{-8}, \pi)$, where $\delta = 2, 4, 6$ and 8 , is possible to ensure chaotic behavior for $k > 0.1$. As detailed in Sec. IIB, for $k \gtrsim 0.1$, a *chaotic layer* surrounds the vicinity of the unstable fixed point at $(0, \pi)$ and, as k increases, the phase space is filled by the expanding chaotic sea. These chaotic trajectories are suitably represented by their respective RPs as depicted earlier by Fig. 4.

Regression results for the Standard map are shown in Fig. 7. Initially in (a), considering the interval $k \in [0.1, k_c)$, the agreement between the predicted and actual parameter values is surprisingly notable for chaotic dynamics. A slight decrease in performance is observed in (b) for parameters beyond the critical value k_c . Although regions above $k > 2.0$ were neglected, these results illustrate that particular finite-time chaotic behaviors, associated with the different values of k , can be successfully predicted with the proposed methodology.

IV. CONCLUSIONS

The main objective of this investigation was to enable effective prediction of non-linear dynamical behaviors in a dynamical system of interest. By evolving the system from given initial conditions and control parameters, the dynamics can be suitably described via recurrence plots. These plots were used to train a neural network capable of recognizing recurrence patterns and distinguishing between behaviors. In this study, two well-known non-linear maps were used to exemplify the use of this methodology. Nevertheless, the presented approach is easily generalized within a broad scope, being readily applicable to real-world phenomena. The presented results, along with the previous works on the classification of chaotic behaviors in the literature, highlight the effectiveness of predicting non-linear dynamics on various dynamical systems.

The chosen CNN architecture proved to be robust to changes in recurrence patterns from both systems, achieving relatively high accuracy in forecasting parameters for both the one-dimensional Logistic map and the two-dimensional Standard map. Notably, performance improvements were observed when focusing training on specific parameter ranges, such as the chaotic regime in the Logistic map or the pre-critical regime in the Standard map. These results suggest that further performance improvements could be achieved through larger sampling sizes and possibly the application of transfer learning strategies.

To further extend the scope of this methodology, future work could explore the use of state-of-the-art archi-

teatures such as ResNet, EfficientNet, and InceptionV3. Training these networks on a large-scale database of RPs, similar to the ImageNet project [30] could enhance the ability to identify real-world dynamical systems. This would enable the neural network to characterize multiple systems and relate them to unknown dynamical behaviors, providing a powerful tool for the classification and prediction of diverse non-linear systems.

ACKNOWLEDGMENTS

Luiza Lober thanks the support given by São Paulo Research Foundation (FAPESP) (grants number 2022/16065-3 and 2013/07375-0). Matheus Palmero also thanks FAPESP (grant number 2023/07704-5). Francisco A. Rodrigues acknowledges CNPq (grant 308162/2023-4) and FAPESP (grants 20/09835-1 and 13/07375-0) for the financial support given for this research.

CODE AVAILABILITY

All data and code used in this work are publicly available at https://github.com/luizalober/chaotic_systems_NN.

Appendix A: Optimal parameters selection

This appendix is devoted to further explore the choice of additional parameters involved in the methodology outlined in Sec. II.

The first objective is to determine the optimal pixel resolution for the RPs used by the main models. To achieve this, several numerical simulations were conducted using different sample sets of varying sizes, with their performances compared. For each comparison, every pixel represented a unique point in the RP, resulting in images with a resolution of $(T \times T)$ pixels, where T denotes the number of iterations in each evolution, as defined earlier in Sec. II A.

The Logistic map was selected for these tests due to its ability to characterize the network's precision across various ranges, thus capturing its well-known behaviors throughout the r range. The training dataset for the neural networks initially consisted of 10^4 unique RP images, generated using uniformly selected values of r , while the hold-out test set contained 500 examples. These sample sizes were fixed across all simulations to manage memory consumption effectively, both in terms of RAM and VRAM, as image resolution increased. The results are presented in Fig. 8.

Considering the lowest values of RMSE for all classes, the optimal resolution is defined as 100×100 pixels, meaning also that the dynamics is evolved up to 100 iterations. This resolution not only allows for the NNs to

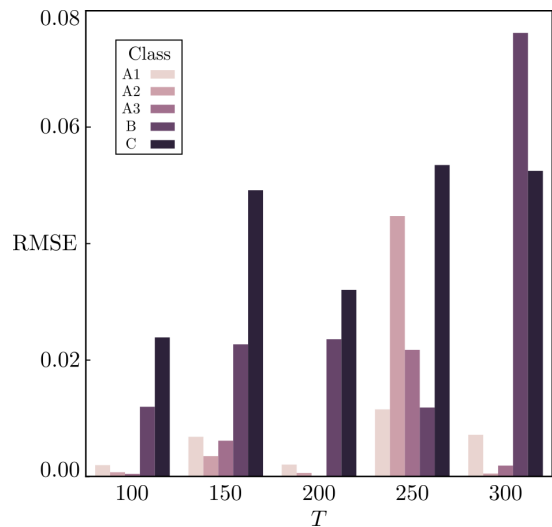


FIG. 8. Results of the Root Mean Square Error (RMSE) considering different maximum iteration number T and, consequently, the RP resolution $(T \times T)$ pixels. The 5 classes are the same as presented in Sec. II B 1.

TABLE III. RMSE and the defined percentage of correct predictions $c(m)$ for the regression tasks considering the Standard map with ICs $(q_0, p_0) = (\delta \times 10^{-\gamma}, \pi)$. Here $\delta = 1.0$ and $k \in [0.1, k_c)$.

γ	RMSE	$c(0.1)$	$c(0.01)$
5	0.0365	98.3%	35.3%
6	0.0347	98.0%	46.9%
7	0.0277	98.9%	45.2%
8	0.0273	99.4%	47.8%
9	0.0410	98.1%	21.8%

efficiently learn the patterns of each class of the Logistic map, but also capitalize on the lower computational cost of the smaller sample sizes to warrant a significant increase in the sampling size of the data, which in turn benefits the learning process of all NNs. Consequently, the sampling was enlarged to contain 4×10^4 unique RP images for the training set, and 10^3 for the hold-out test set, which is the same sampling size used for the final results, as discussed in Sec. III.

An argument can also be made for the increased complexity of the dynamics when considering higher resolutions, which result from allowing for more iterations of the maps. These more complex RPs can compromise the efficiency of the pattern recognition capability of the NNs, which is especially true for chaotic behavior as observed in classes B and C in Fig. 8. Indeed, Fig. 9 illustrates the compression of such patterns in an increasing pixel resolution and, consequently, maximum iteration time T .

The next additional parameter that needs to be carefully selected is order γ for the distance between the pair of ICs $(q_0, p_0) = (\delta \times 10^{-\gamma}, \pi)$ and the unstable fixed point at $(0, \pi)$ in the Standard map. Since only chaotic

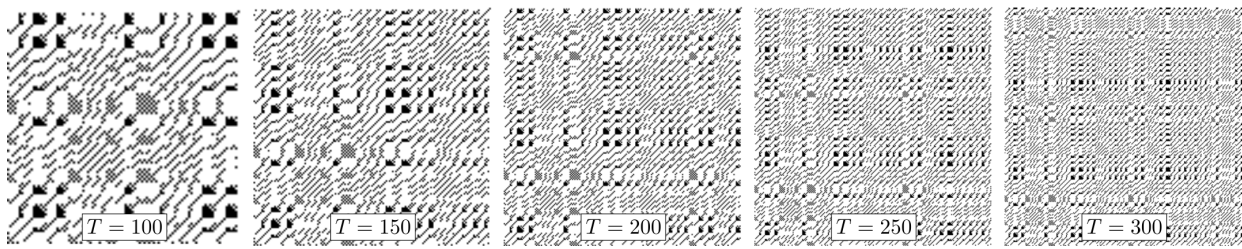


FIG. 9. Five examples of RPs with increasing maximum iteration time T and, consequently, their resolution ($T \times T$ pixels). Here the Logistic map is evolved with fixed IC $x_0 = 0.1$ and control parameter $r \approx 3.7004$.

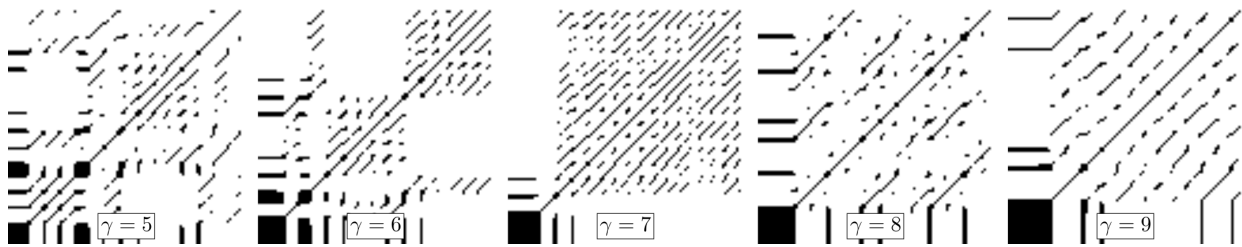


FIG. 10. Five examples of RPs considering the Standard map with fixed control parameter $k \approx 0.97137$ and ICs $(q_0, p_0) = (\delta \times 10^{-\gamma}, \pi)$. Here $\delta = 1.0$ while varying the order γ , evolving these five trajectories up to $T = 100$ iterations.

dynamics is analyzed in this case, it is fair to assume that the optimal resolution would be the same as previously chosen for the Logistic map, especially considering the low RMSE for the region of chaotic behavior, namely B and C classes. With that, several simulations were performed considering the range of the characteristic control parameter $k \in [0.1, k_c)$, a fixed $\delta = 1$ and different values for the order $\gamma = 5, 6, 7, 8$ and 9. The results of RMSE and the percentage of correct predictions $c(m)$ are presented in Tab. III.

From the comparison of the results presented in Tab. III, $\gamma = 8$ was chosen as the optimal order, meaning that the pair of ICs (q_0, p_0) is effectively selected as $(10^{-8}, \pi)$. As discussed in detail in Sec. II B, this special pair of ICs warrants chaotic dynamics even for relatively small values of the control parameter k , allowing a suitable comparison between different behaviors within Hamiltonian chaos. Nevertheless, the results shown in Tab. III are ex-

pected, but also intriguing. On the one hand, RMSE values should indeed be inversely proportional to γ , meaning that the closer the ICs are to the unstable fixed point, the NN would be able to recognize even more different chaotic behaviors. On the other hand, $\gamma = 9$ produces an unexpected outcome, since it should be the lowest value of RMSE and $c(m)$. This result is still unclear and will be addressed in future works.

Finally, Fig. 10 exemplifies the differences between the RPs of the Standard map considering different orders of γ for the pair of ICs. It is worth noting that, as expected, the size of the initial black square increases as γ also increases, showing the influence of the unstable fixed point at the beginning of the dynamical evolution. Moreover, as an additional subject for future investigations, the rate of expansion of the black square for increasing γ might be inherently connected to the local Lyapunov exponent associated with these chaotic trajectories.

-
- [1] S. H. Strogatz, *Nonlinear Dynamics and Chaos: With Applications to Physics, Biology, Chemistry and Engineering* (Westview Press, 2000).
 - [2] D. E. Stewart and R. L. Dewar, Non-linear dynamics, in *Complex Systems*, edited by T. R. J. Bossomaier and D. G. Green (Cambridge University Press, 2000) p. 167–248.
 - [3] G. Zaslavsky, *Weak Chaos and Quasi-Regular Patterns*, Cambridge Nonlinear Science Series (Cambridge University Press, 1992).
 - [4] A. J. Lichtenberg and M. A. Leiberman, *Regular and Chaotic Dynamics* (Springer Berlin Heidelberg, 1992).
 - [5] E. Ott, *Chaos in Dynamical Systems* (Cambridge University Press, 2002).
 - [6] G. Zaslavsky, *Chaos in Dynamic Systems* (Harwood Academic Publishers, 1985).
 - [7] S. Wiggins, *Introduction to Applied Nonlinear Dynamical Systems and Chaos*, Texts in Applied Mathematics (Springer New York, 2003).
 - [8] A. Shrestha and A. Mahmood, Review of Deep Learning Algorithms and Architectures, *IEEE Access* **7**, 53040 (2019).
 - [9] S. Cong and Y. Zhou, A review of convolutional neural network architectures and their optimizations, *Artif. Intell. Rev.* **56**, 1905 (2023).
 - [10] Z. Li, F. Liu, W. Yang, S. Peng, and J. Zhou, A Sur-

- vey of Convolutional Neural Networks: Analysis, Applications, and Prospects, *IEEE Trans. Neural Networks Learn. Syst.* **33**, 6999 (2021).
- [11] Y. Zhou, S. Gao, M. Sun, Y. Zhou, Z. Chen, *et al.*, Recognizing Chaos by Deep Learning and Transfer Learning on Recurrence Plots, *Int. J. Bifurcation Chaos* **33**, 2350116 (2023).
- [12] J. Nam and J. Kang, Classification of Chaotic Signals of the Recurrence Matrix Using a Convolutional Neural Network and Verification through the Lyapunov Exponent, *Appl. Sci.* **11**, 77 (2020).
- [13] C. L. Webber Jr and J. P. Zbilut, Recurrence quantification analysis of nonlinear dynamical systems, *Tutorials in contemporary nonlinear methods for the behavioral sciences* **94**, 26 (2005).
- [14] N. Marwan, M. C. Romano, M. Thiel, and J. Kurths, Recurrence plots for the analysis of complex systems, *Physics Reports* **438**, 237 (2007).
- [15] N. Marwan and K. H. Kraemer, Trends in recurrence analysis of dynamical systems, *The European Physical Journal Special Topics* **232**, 5 (2023).
- [16] R. V. Donner, M. Small, J. F. Donges, N. Marwan, Y. Zou, R. Xiang, and J. Kurths, Recurrence-based time series analysis by means of complex network methods, <https://doi.org/10.1142/S0218127411029021> **21**, 1019 (2011).
- [17] C. Webber and N. Marwan, *Recurrence Quantification Analysis – Theory and Best Practices* (Springer, 2015).
- [18] B. Goswami, A brief introduction to nonlinear time series analysis and recurrence plots, *Vibration* **2**, 332 (2019).
- [19] T. L. Prado, G. Corso, G. Z. dos Santos Lima, R. C. Budzinski, B. R. R. Boaretto, F. A. S. Ferrari, E. E. N. Macau, and S. R. Lopes, Maximum entropy principle in recurrence plot analysis on stochastic and chaotic systems, *Chaos: An Interdisciplinary Journal of Nonlinear Science* **30**, 043123 (2020).
- [20] T. D. Pham, Fuzzy recurrence plots, in *Fuzzy Recurrence Plots and Networks with Applications in Biomedicine* (Springer International Publishing, Cham, 2020) pp. 29–55.
- [21] M. S. Palmero, I. L. Caldas, and I. M. Sokolov, Finite-time recurrence analysis of chaotic trajectories in hamiltonian systems, *Chaos: An Interdisciplinary Journal of Nonlinear Science* **32**, 113144 (2022).
- [22] E. D. Lorenz, The problem of deducing the climate from the governing equations, *Tellus A: Dynamic Meteorology and Oceanography* **16**, 1 (1964).
- [23] R. May, Simple mathematical models with very complicated dynamics, *Nature* **26**, 457 (1976).
- [24] B. V. Chirikov, *Research concerning the theory of nonlinear resonance and stochasticity*, Tech. Rep. (CM-P00100691, 1969).
- [25] B. V. Chirikov, A universal instability of many-dimensional oscillator systems, *Phys. Rep.* **52**, 263 (1979).
- [26] R. MacKay and J. Meiss, *Hamiltonian Dynamical Systems: A REPRINT SELECTION* (CRC Press, 1987).
- [27] J. M. Greene, A method for determining a stochastic transition, *Journal of Mathematical Physics* **20**, 1183 (1979), https://pubs.aip.org/aip/jmp/article-pdf/20/6/1183/19001735/1183_1_online.pdf.
- [28] R. MacKay, A renormalization approach to invariant circles in area-preserving maps, *Physica D: Nonlinear Phenomena* **7**, 283 (1983).
- [29] M. Abadi, A. Agarwal, P. Barham, E. Brevdo, Z. Chen, C. Citro, G. S. Corrado, A. Davis, J. Dean, M. Devin, S. Ghemawat, I. Goodfellow, A. Harp, G. Irving, M. Isard, Y. Jia, R. Jozefowicz, L. Kaiser, M. Kudlur, J. Levenberg, D. Mané, R. Monga, S. Moore, D. Murray, C. Olah, M. Schuster, J. Shlens, B. Steiner, I. Sutskever, K. Talwar, P. Tucker, V. Vanhoucke, V. Vasudevan, F. Viégas, O. Vinyals, P. Warden, M. Wattenberg, M. Wicke, Y. Yu, and X. Zheng, TensorFlow: Large-scale machine learning on heterogeneous systems (2015), software available from tensorflow.org.
- [30] J. Deng, W. Dong, R. Socher, L.-J. Li, K. Li, and L. Fei-Fei, ImageNet: A Large-Scale Hierarchical Image Database, in *CVPR09* (2009).